William Marsh Rice University
Department of Earth Science MS-126
6100 South Main Street
Houston TX 77005

Sulfide Dissolution Rates Studied by Vertical Scanning Interferometry: Comparison with and Application to Studies in Laboratory and Natural Setting (Final Technical Report)

Andreas Luttge[1] and Rolf S. Arvidson[1]

Preamble

This report is presented in compliance with and satisfaction of reporting requirements for the Mineral Resources External Program (USGS-MRERP, project award #06HQGR0175). The research described here was completed at the Department of Earth Science at Rice University, and represents the work product of the authors as well as the following Rice University graduate students and postdoctoral research staff: Carter Sturm, Michael Vinson, Li Zhang, and Cornelius Fischer. This work also contains results of collaborative activities between the authors at Rice University and Jordi Cama[2] and M. Pilar Asta[2].

The following publication has resulted from this research: Asta MP, Cama J, Solera JM, Arvidson RS and Lüttge A, Interferometric study of pyrite surface reactivity in acidic conditions. Amer. Mineral., *in press*.

Required Statement:

"Research supported by the U.S. Geological Survey (USGS), Department of the Interior, under USGS award number #06HQGR0175. The views and conclusions contained in this document are those of the authors and should not be interpreted as necessarily representing the official policies, either expressed or implied, of the U.S. Government."

Introduction

The effects of acid mine drainage have been extensively documented in the United States, and has been described as a primary source of surface water contamination and degradation of surface environment quality (United States EPA, 1994). The oxidation and subsequent weathering of sulfide minerals releases metals, sulfur, and acid to the surrounding aqueous environment, resulting in contamination and despoiling of surface and ground waters, soils, and sediments, and bioaccumulation of metals in wildlife and domestic stock. In addition to field characterization, there has also been considerable effort devoted to investigation of reaction mechanism, with common dependencies on oxygen concentration, pH, and Fe^{III} (Smith and Shumate, 1970; Singer and Stumm, 1970; McKibben, 1984; McKibben and Barnes, 1986; Nicholson et al., 1988; Moses and Herman, 1991; Williamson and Rimstidt, 1994; Rimstidt and Vaughn, 2003).

Reaction mechanism, pH, and oxygen – It is critical to recognize that the dissolution of pyrite often occurs in association with the dissolution of other base metal sulfides as well (Rimstidt et al., 1994). The dissolution of these phases may proceed via a range of possible reactions, including simple non-oxidative hydrolysis, or oxidation by either oxygen or ferric iron. This diversity in reaction paths may lead to parallel or coupled processes, whose interaction produce complex feedback effects that determine the behavior of

[1] Department of Earth Science MS-126, Rice University, Houston Texas USA 77005
[2] Department of Environmental Geology, Institute of Earth Sciences "Jaume Almera", CSIC, Lluís Solé i Sabarís s/n, 08028, Barcelona, Catalonia, EU

the system as a whole. Stanton et al. (2005) have shown that sphalerite dissolution displays a complex dependence on Fe^{III} availability, pH, dissolved oxygen, and the iron content of the mineral itself. At low pH, Stillings et al. (2005) have shown that pH variation, as opposed to oxygen availability, is the dominant control on the release of Cu and Fe from chalcopyrite dissolution. Recent studies of pyrite oxidation (e.g., Seal and Rimstidt, 2005) reveal complex pH-dependent relationships involving the early transfer of sulfur to solution, and suggest that the availability of other metal ligands (e.g., copper) may catalyze overall oxidation. Thus oxidative coupling in terms of electron and proton exchange in these reactions determines both the total load and distribution of metal output. A general, empirical rate law for the dissolution of pyrite and other metal sulfides can be written to describe the role of these components (cf. McKibben and Barnes, 1986; Nicholson et al, 1988; Moses and Herman, 1991; Williamson and Rimstidt, 1994; Domènech et al., 2002) as

$$r = k\,(O_{2\,(aq)})^{n1}\,(Fe^{III})^{n2}\,(a_{H}{}^{+})^{n3}$$

where r is the overall rate in units of mols per unit area per unit time, k is the overall rate constant, $O_{2\,(aq)}$ and Fe^{III} are the concentrations of dissolved oxygen and ferric iron, and $a_{H}{}^{+}$ is the proton activity, parameterized by the corresponding empirical constants n_1, n_2, and n_3.

Approach using Vertical Scanning Interferometry – Much of the earlier laboratory work on sulfide dissolution has been devoted to a description of the rate described in eq [1] using conventional methods, where reaction rate is determined by changes in solution composition (McKibben and Barnes, 1986; Nicholson et al, 1988; Moses and Herman, 1991; Williamson and Rimstidt, 1994; Domènech et al., 2002). A more recent suite of studies has focused primarily on the study of elementary processes at the atomic scale on pyrite surfaces (e.g., Roso and Vaughan, 2006). Following the approach with which we have had fundamental success over the past several years (e.g., Lüttge et al. 1999, 2005; Arvidson et al., 2003, 2006), we have used vertical scanning interferometry (VSI) to explore the general problem of reactivity and reaction mechanism of pyrite surfaces. To summarize briefly here, the scanned surfaces are on the order of tens of thousands square microns, in comparison with scans of few tens of microns provided by the AFM. This gives precise dissolution information relevant to surface mechanisms over characteristic areas of the reacted surface. Also, the nanoscale precision of the vertical measurements allows accurate determination of variation in size and shape of the reactive surface features (etch pits, steps, terraces, etc.). Mineral dissolution rates are measured directly from variations in surface height with time, using either the total surface explored or at specific locations. This means that rates values obtained are true dissolution rate values derived independently of externally measured surface areas, such as BET specific surface area or geometric surface area, thus avoiding the introduction of a rate normalization factor. Lastly, the metallic properties of sulfide minerals provide excellent light reflection, which makes VSI an ideal technique to explore the pyrite surface reactivity.

This paper has three goals. The first goal is to resolve the surface reaction mechanisms for pyrite dissolution at undersaturated conditions. The second goal is to obtain, for the first time, the dissolution rate of pyrite by means of VSI measurements. A weathered pyrite surface has been selected to carry out the VSI measurements with the purpose of approximating conditions at the mineral surface in a natural weathering environment. Although pyrite has a poor (100) cleavage, its structural simplicity (FeS_2) makes this mineral a feasible choice with which to test the predictions of the stepwave model, and a useful starting point from which to conduct further VSI work on sulfide-solution interface reactivity. The third goal, based on the dissolution of a pyrite fragment, is to derive the dissolution rate by normalizing to the geometric surface area, and compare these data with the pyrite dissolution rate calculated by VSI measurements (e.g., direct approach), together with rates reported in the literature that are obtained from bulk measurements normalized to the BET surface area (indirect approach).

EXPERIMENTAL METHODOLOGY

Sample characterization – Pyrite for all experiments was obtained from surface outcrops in the Catalan Pyrenees Range (Iberian Peninsula). These samples have already been exposed to weathering under field conditions, allowing us to investigate the surface changes on weathered surfaces under laboratory conditions. Selected areas were scanned prior to dissolution experiments. Changes in surface topography

arising from dissolution could then be resolved by comparing these data with those obtained after dissolution.

Experiments were conducted under flow and static conditions (in contact with lab atmosphere). For the flow reactor experiment, a pyrite fragment (6×2.5×0.4 mm) was obtained by cutting from a larger sample. For the purpose of estimating surface area we assumed all faces of this sample to be flat. The cutting process generated micron-sized particles adhering to and non-uniformly distributed over the surface. However, our estimate of the areal contribution of these particles was within the error of our estimate of the geometric surface of the sample (3.7×10^{-5} m^2). This area was used to normalize the dissolution rate (mol m^{-2} s^{-1}) obtained by means of the dissolved fragment.

VSI experimental setup – We used a vertical scanning interferometer (MicroXam, ADE Phase Shift) with 10× Mirau objective and a white light source to quantify the dissolution processes. At this magnification (840×640 micron field of view), the vertical resolution of the system is better than 2 nm, with a lateral resolution of ~1 micron. By protecting a reference area with an inert silicone mask, absolute height measurements were obtained by revisiting the same area on the surface. Changes in surface topography were quantified by comparison of digital interferograms collected at successive intervals in the experiment. These surface data are rendered as topographic maps using SPIP (Image Metrology A/S).

For the static experiments, sample fragments were suspended in a 10 L polypropylene bottle containing a pH 1 (HCl) solution and allowed to dissolve for 27 days under atmospheric conditions (PO_2 0.21 atm) and room temperature (22 ± 2°C). The low solid/solution ratio and slow dissolution rate of pyrite ensured that reaction occurred under highly undersaturated conditions with respect to pyrite. Variation in total iron and total sulfur was monitored during the experimental run.

After the desired reaction time, a fragment was withdrawn from solution, dried with compressed air (2-3 min) at room temperature, and mounted on a sample holder for the interferometer analyses. These *ex situ* measurements required ~2 hours, after which the sample was returned to the bottle with the same solution to continue its dissolution. The selected surface was examined after 13, 21, and 27 days of reaction time, together with a solution aliquot (5 mL) for total dissolved iron and sulfur determinations. It was assumed that at pH 1 the aqueous concentration of Fe(II) is that of total iron (Singer and Stumm, 1970) and that total sulfur corresponds to sulfate (Bonnissel-Gissinger et al., 1998). The saturation index of the solution ((SI = $\log(IAP/K_{eq})$, where IAP is the ion activity product) was calculated along the experiment at 25°C using the PHREEQC code (Parkhurst 1995) and the database MINTEQ. The other fragment was only retrieved and examined after 27 days. The silicon rubber was removed from the covered spots and the vertical changes with the use of reference surfaces were quantified. Using the SPIP software, digitized interferograms of the sample surface were converted to height-mode and three-dimensional images.

Flow reactor setup – The pyrite fragment was suspended inside a flow-through Lexan reactor (ca. 35 mL in volume) at pH 1, O_2 saturated atmosphere and room temperature (22 ± 0.2 ºC). The flow rate was maintained constant at 0.03 mL min^{-1}. Once the steady state was attained, the dissolution rate, r_{geo} (mol m^{-2} s^{-1}), was calculated from the release of Fe according to the expression

$$r_{geo} = q / A \, C_{Fe,out}$$

where $C_{Fe,out}$ is the total concentration of iron in the output solution, (mol m^{-3}), A is the geometric surface area of the fragment (m^2) and q is the volumetric flux of fluid through the system (m^3 s^{-1}). In this experiment the error associated with the dissolution rate can reach 21% as the estimated value of geometric surface area has an associated error of about 15% and the analytical error of iron concentration is about 15%.

Solution – Input solutions were prepared with Millipore MQ water (18 MΩ·cm) at pH 1 and HCl reagent (Merck). Input solution pH and solution pH along the experiments were measured with a Crison© combined glass electrode at room temperature (22 ± 2 ºC), yielding pH 1.01 with an error of 0.02 pH units. Total concentrations of Fe and S from output solutions were determined by inductively coupled plasma atomic

emission spectroscopy (ICP-AES). The measured output Fe concentrations ranged between 0.6 and 1.4 μM with an associated error of around 15% and the S concentrations were below detection limit (3.5 μM).

VSI dissolution rates – Interferometry measures relative surface height. By maintenance of a reference (unreacted) surface on the mineral itself, this measurement becomes absolute (Luttge et al. 1999; Arvidson et al. 2003). The lateral (*x, y*) resolution of this height measurement is a function of the objective magnification, CCD camera pixel size, and the wavelength of the reflected light; these instrument parameters are matched to provide optimal resolution. Each camera pixel records a single, discrete height (h_{ij}), and this value accurately reflects the *mean* height of the actual mineral surface over the area of a single pixel. At 50× magnification, the objective used for all height measurements, the lateral resolution is ~ 0.5 μm (using a data pixel density of 740×480 and a field of view of 165 μm×124 μm). The instrument is capable of routinely resolving subnanometer height differences. The heights h_{ij} collected at all pixels are averaged over the entire field of view to provide an average surface height ($\bar{h}$) relative to a level datum. During dissolution, surface height is lost as the surface retreats, and thus changes in average height $\Delta \bar{h}$ made at timed intervals (Δt) yield a retreat velocity:

$$v_{[hkl]} = \Delta \bar{h} \; / \Delta t$$

Integrating h_{ij} over the area of each pixel yields a total volume of material removed per unit time:

$$V_{diss} = \sum_j \sum_i a_{ij} h_{ij} = A \sum_j \sum_i h_{ij}$$

Dividing the velocity in [3] by the molar volume V_m (pyrite, 23.94 cm^3 mol^{-1}) gives a dissolution rate in the familiar units of moles per unit area per unit time:

$$r = v_{[hkl]} / V_m$$

This approach allows a simple and straightforward quantification of absolute dissolution rates from VSI measurements of surface height, fully incorporating the fact that reactivity is site-specific and thus varies with surface location. It is also important to note that given the subnanometer vertical resolution of this system and the duration of the VSI experiments (27 d), the smallest detectable increase in height yields a dissolution rate of 1.7×10^{-11} mol m^{-2} sec^{-1}. Rates associated with undetectable height variation result in negligible dissolution rates.

Surface roughness variation – VSI also permits quantification of surface roughness in both two dimensions (i.e. a surface profile over a transecting line) and three dimensions (integrated surface profiles, i.e. a complete surface scan). These parameters were computed according to standard parameter definitions (e.g., Thomas, 1999).

RESULTS AND DISCUSSION

Weathered pyrite surface – The weathered pyrite surface was characterized by (100) terraces of limited lateral extent having steps of 0.2 to 3 micrometer in height (Figure 1a). The distribution of etch pits was highly varied: densely pitted regions (1 to 9×10^5 pits nm^{-2}, with depths up to 400 nm, Figure 1b,c) contrasted with regions lacking pits entirely. However, the variation in etch pit density (between 0 and 2×10^5 pits nm^{-2}) is only weakly reflected in surface roughness (Figure 1d,e). These relationships, reflecting the fact that differences in surface reactivity may be both the cause and effect of this morphological heterogeneity on the pyrite surface, are discussed below.

Dissolution mechanisms – In order to characterize the surface, two representative portions of pre- and post-reacted surfaces were chosen that fully represented the variation in surface features defining the surface topography. Comparison of these regions illustrates the progress of the dissolution process over the pyrite surface (). The first portion shows a region composed of two, flat terraces (Figure 2a). The two terraces, the

upper terrace (A) and the foreground terrace (B), are initially pitted with etch pits that are either isolated or forming clusters. Pit depths range from tens to hundreds of nanometers. (Figure 2b,c) show the effect of dissolution on both terraces through the experiment. After 27 d of reaction, the intensity of dissolution attack on terrace (A) appears to be higher than in terrace (B). On terrace A the growth of the isolated pits and increase in clusters of pits is observed. In terrace B the little change of topography is the nucleation of a few shallow etch pits (lower right-hand corner on Figure 2b,c). It appears then that the variation in topography of terrace (A) can be distinguished when compared to that of terrace (B), where surface remained practically invariable. Figure 2d-f show terrace (A) in more detail; as the increase in etch pit density occurred due to pit nucleation and clustering, pit coalescence happened simultaneously. As a result, retreat of the surface perpendicular to the terrace plane was observed in this part of the surface (Figure 2f).

A detailed inspection of the etch pit evolution shows that the initial etch pits grew in depth and size (Figure 3). Shapes of initial pits are not angular and show rounded boundaries (indicated as P in Figure 3a). Nucleation of new etch pits yields pits with similar shape and variability in depth. The “growth” of the existing etch pits and the formation and “growth” of new ones result in a widespread pit coalescence, i.e., pits that grow larger annihilate each other. It appears that this surface phenomenon is promoted from the etch pit boundaries, which are an efficient source of steps. As the steps move out, a train of steps result in an overall surface retreat (see arrows S in Figure 3b). This hypothesis would be in agreement with the kinetic theory proposed by Lasaga and Luttge (2001) that states that under large undersaturation etch pits open up and are the source of a train of steps, leading to dissolution stepwaves that control the bulk mineral dissolution. Note that in the conducted experiment the concentrations of total sulfur and total iron were lower than 3.5×10^{-6} M. As indicated before, assuming that at pH 1 total iron is mainly Fe(II) and total sulfur is sulfate the log saturation index is −3.7. This indicates that pyrite dissolution took place under highly undersaturated conditions with respect to pyrite.

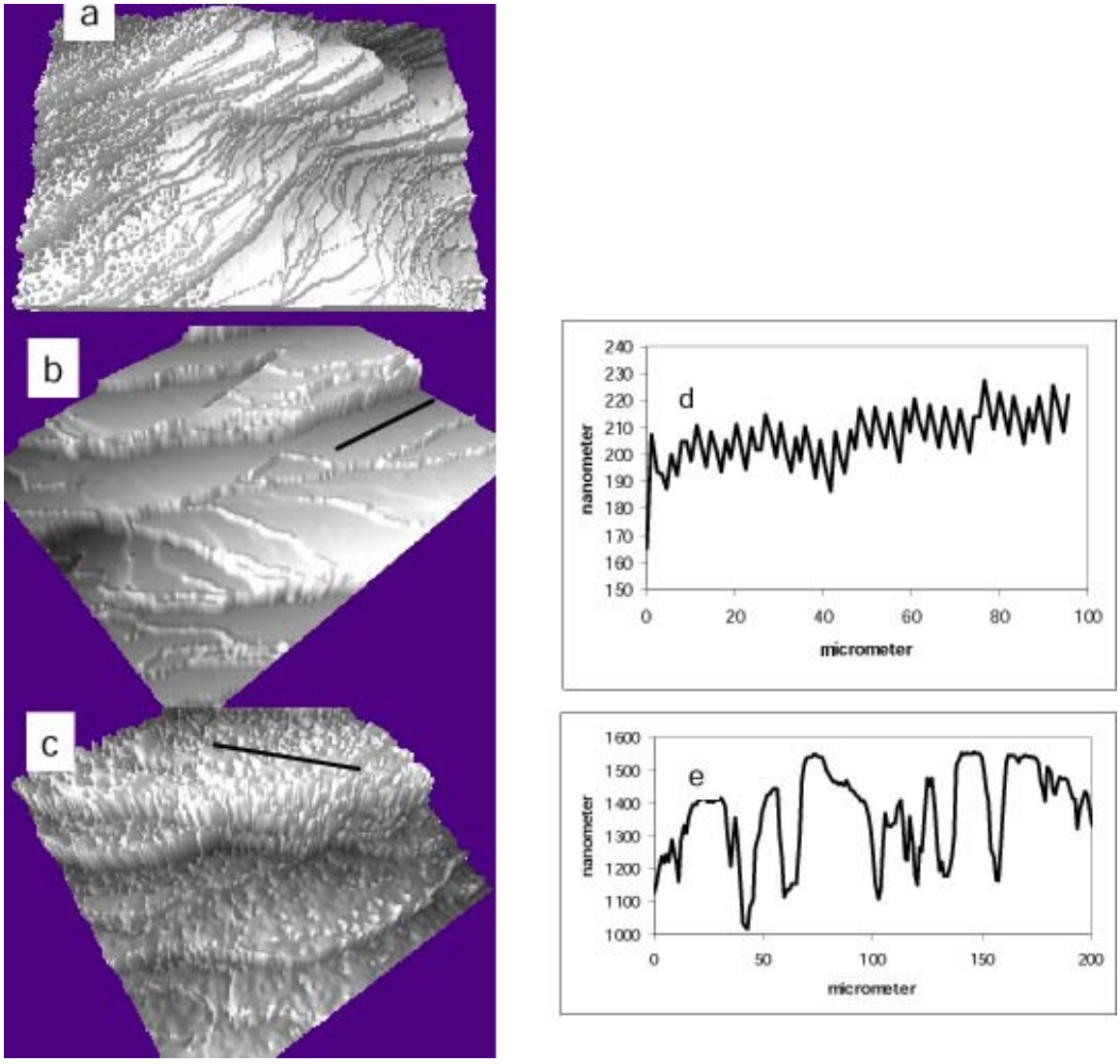

Figure 1. Weathered surface of pyrite. Three-dimensional views of (a) a 500×400 micrometer region, where the terraces that define the surface topography are readily visible; (b) 250×200 micrometer region that is composed of pit-free terraces; and (c) 300×300 micrometer region, composed of densely pitted terraces. The height between terraces ranges from 100 nm to 2 microns. The line profile in (d) corresponds to surface terrace in (b), showing shallow pits (about 10 nm), and line profile in (e) is from terrace in (b) with deep pits (depth of the etch-pits ranges from 100 to 500 nm). Note that units in the Y and X axes are 618 nm and μm, respectively.

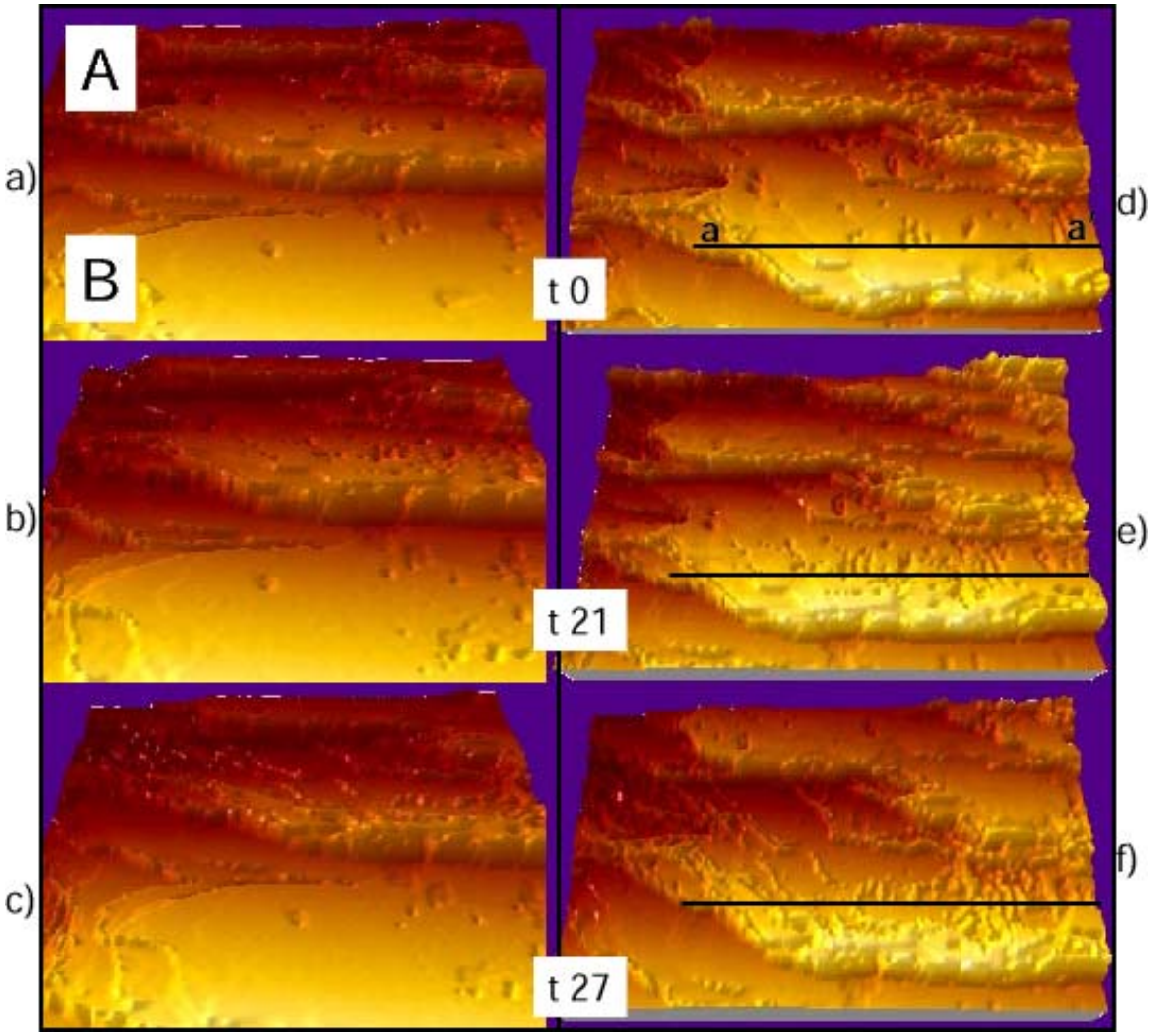

Figure 2. Three-dimensional images of the surface that shows the presence of two terraces (A and B), separated by a step (ca. one μm in height), and scattered pits over the surface area, either isolated or clustered: Initial surface (a); After 21 (b) and 27 days (c) of dissolution in HCl solution (pH 1) at room temperature and oxygen saturated atmosphere. Image dimensions are 250×125 μm. 180×90 μm images from (d) to (f) show the surface evolution in terrace A; Formation of new etch pits, pit clustering, pit coalescence and surface retreat are observed. Lines indicate line profiles (see Figure 4).

The topographic variation in the line profiles with time in Figure 4 is useful to show the dynamic characteristics of reactive features that dominate the dissolution process (growth and formation of etch pits, etch-pit coalescence and surface retreat) on terrace A (Figure 2 and Figure 3). During the first stage of reaction, it appears that some initial deep pits grow in depth, and that isolated shallow pits dissolve extensively (points 1, 2 and 3 in Figure 4a). Thus pit deepening and pit nucleation occur. This surface evolution is promoted by steps moving out from the pit boundaries. It is important to note that in the line profiles lengths on the Y-axis versus the X-axis are exaggerated (nm versus μm, respectively). For example, as a pit of 200 nm in depth formed, steps travelled tens of micrometers from the pit's boundaries. Therefore, step spreading over the surface normal to pit deepening predominates. Figure 4b shows the surface retreat in an intermediate stage between the initial and final surfaces. Trains of steps must be responsible of such a surface variation. This surface retreat is shown in Figure 4c. We can thus infer that pyrite dissolution in this particular surface region proceeds as described by the stepwave model (Lasaga and Luttge, 2001).

The second section of the surface selected to illustrate the pyrite dissolution mechanisms is exhibited in Figure 5a. This surface portion is densely pitted. After 13 d of dissolution variation in surface topography is readily observed (Figure 5b). Two different profiles are shown; the upper profile of the image shows that surface retreat was taking place in this terrace (Figure 5c), whereas formation of etch pits was the dominant dynamic feature in the lower terrace (Figure 5d).

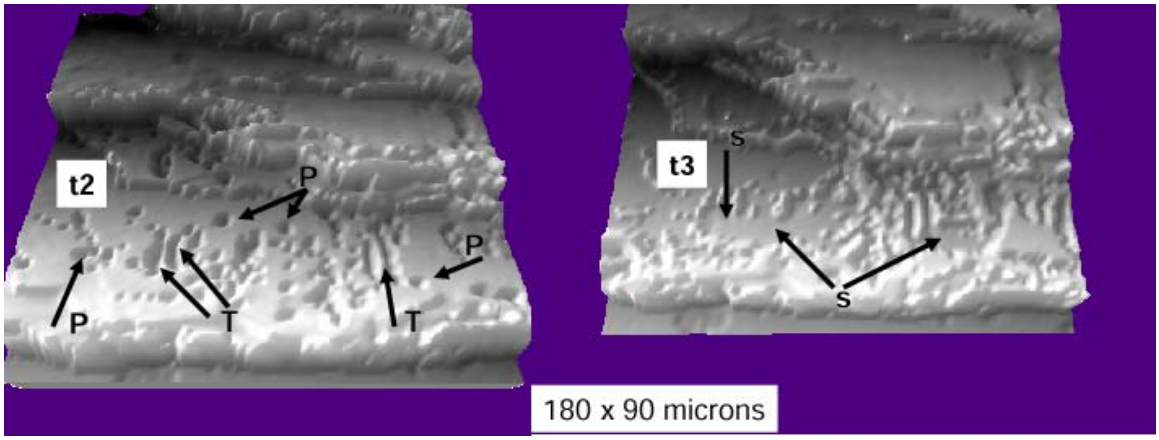

Figure 3. Three-dimensional images of the reactive features on terrace A after 21 d (t2) and 27 d (t3). **P** indicates rounded boundaries of etch pits, **T** indicates a train of coalescent etch pits, and **S** indicates surface retreat. Surface dimensions are 180×90 microns.

Therefore, a comparison of the two selected surface sections suggests that initially different surface features lead to differences in subsequent dissolution, as determined by the underlying mechanism. This suggests that even though an average dissolution rate could be calculated for the whole surface, dissolution occurs heterogeneously on weathered surfaces. This experimental evidence is only observable if the analytical surface is sufficiently large and if a naturally weathered surface is examined. It is therefore not surprising that dissolution rates estimated by local variation in surface topography do not represent the overall dissolution rate (Cama et al., 2005).

Figure 6 exhibits another surface portion selected to illustrate how the dissolution kinetics are dominated, at this stage, by the coalescence of individual pits in the upper part of the region and local annihilation of etch pits in the lower part. In this case, coalescence of pits is extensive (upper part) but not uniform (right lower corner). The profiles in Figure 6 show that at subsequent stages (t2 and t3) pit deepening is imperceptible and that the boundary of the etch pit moves away as predicted by the stepwave model.

The overall pattern of dissolution detectable at 10× (with 700×700 micron FOV) after 13, 21 and 27 days can be summarized as (1) formation of isolated etch pits at the very early stages of dissolution, followed by (2) successive coalescence of pits over time. This process results in net surface retreat, detectable as differences in surface height between masked and unmasked regions. This pattern is consistent with the dissolution stepwave model, in which step trains propagating from nascent etch pits nucleated at screw dislocations travel across the surface and result in net mass removal. The coupled processes of etch pit growth and coalescence, stepwave migration, and nucleation of new pits result in a dynamic, non-steady-state surface topography.

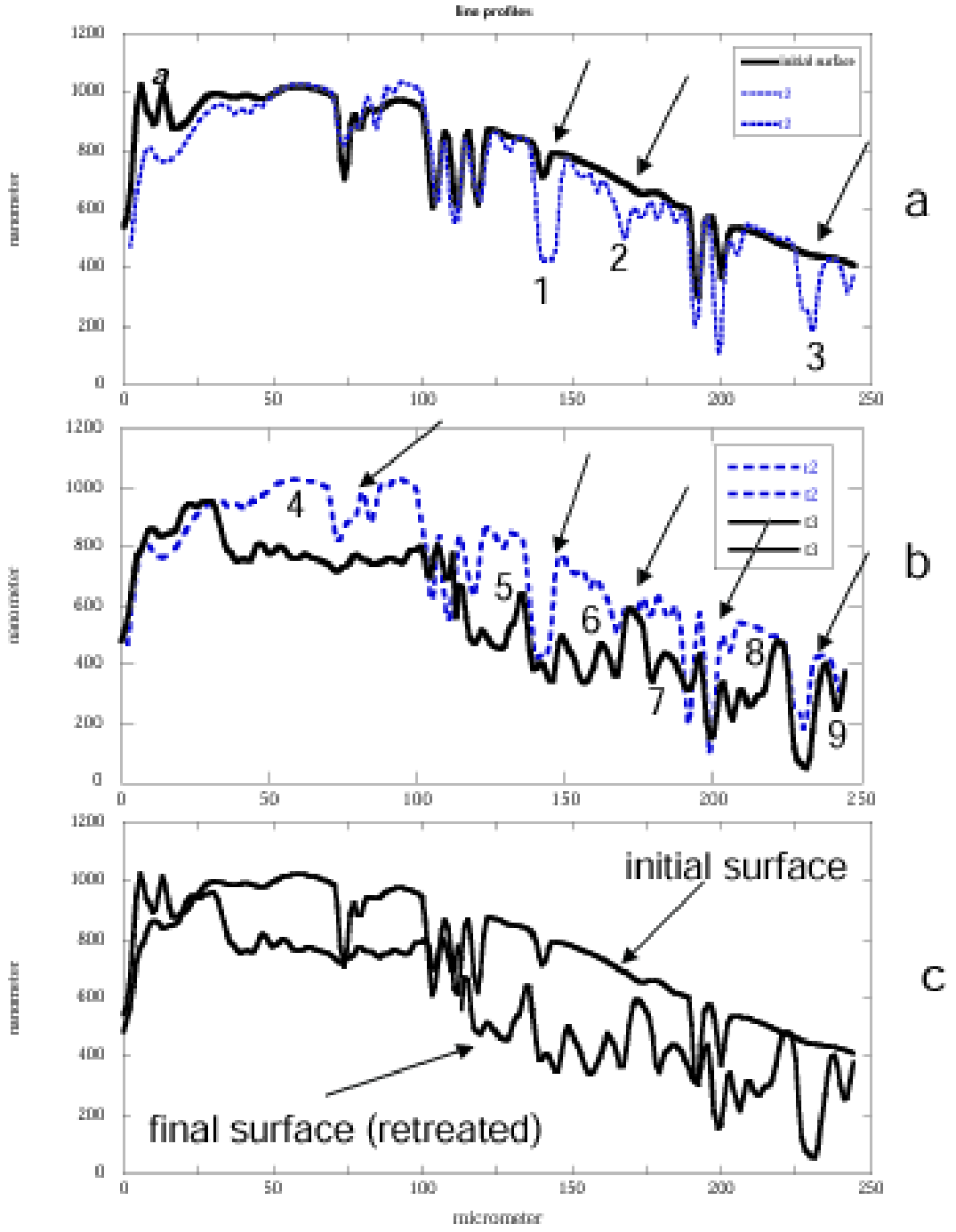

Figure 4. Line profiles as depicted in Figure 2. (a) t0 (initial surface) and t2 (21 d); (b) t2 (21 d) and t3 (27 d); (c) initial surface and final surface showing surface retreat after 27 d of reaction. Arrows indicate surface spots in which etch pit formation occurred and drove the surface retreat consistent with the stepwave mechanism. Numbers indicate the areas used to calculate the dissolution rates based on height variation.

Pyrite dissolution rate and surface reactivity – In the first portion of the surface selected, dissolution rates are calculated from the topographic height change at local surface spots after 27 d based on the surface-normal rate [eq 5]. Figure 4 depicts the surface evolution in a line profile. The rate values vary by a factor of 3, from 1.9×10^{-9} to 6.5×10^{-9} mol m^{-2} sec^{-1}. This suggests that the dissolution rate is variable at the submicron scale. This local variation could stem from the variation in individual step velocity associated with each etch-pit evolution, although an average dissolution rate must control the bulk pyrite dissolution.

In the profiles of Figure 5 (second portion of the surface), the normal velocity estimated in the selected reference points was 7.6×10^{-9} mol m^{-2} sec^{-1} (e.g. surface retreat) and 5.3×10^{-9} mol m^{-2} sec^{-1} (e.g. pit deepening). These velocities are close enough to suggest that the velocities of surface retreat and pit deepening were practically the same, at least over this portion of the pyrite surface.

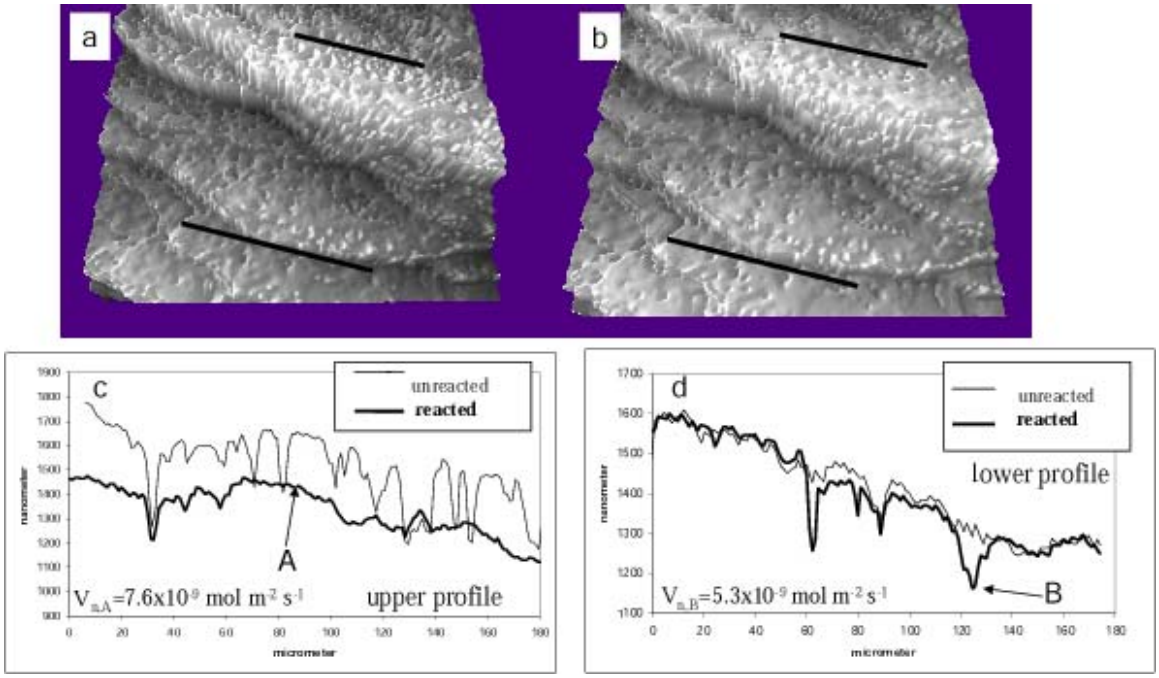

Figure 5. Three-dimensional images of (a) initial surface with different pit distribution and (b) reacted surface after 13 d (t1) showing the formation of a large etch pit due to coalescence. Images are 250×250 microns. The profiles in (c) and (d) exhibit distinct surface evolution (t1-t3).

Nonetheless, reactivity was not uniform all over the surfaces, as observed in the three regions selected (Figures 3-6), where zones in these regions did not develop pits or show surface retreat. This non-uniform reactivity is shown in Figure 7 where surface regions with their associated dissolution rate are exhibited. It is important to highlight that rates vary from "zero" to 1.7×10^{-7} mol m^{-2} sec^{-1}. Thus, 58 % of the total area dissolved less than the detectable rate or very slowly. Figure 7b shows that 3.2 % of the total area scanned dissolves either at "zero" rate or very slowly, e.g., $r = 1.7 < 10^{-11}$ mol m^{-2} sec^{-1}. Figure 7c shows that 25 % of the total area dissolves between 1.7×10^{-11} and 1.7×10^{-9} mol m^{-2} sec^{-1}. Figure 7d shows that only 14 % of the total area dissolves very rapidly, e.g., $1.7\times10^{-8} < r < 1.7\times10^{-7}$ mol m^{-2} sec^{-1}. Averaging the rates of these regions, the average dissolution rate for the pyrite surface investigated is 2.8×10^{-9} mol m^{-2} sec^{-1}. Luttge et al. (1999) raised the argument as to whether the average dissolution rate estimated from the entire surface by averaging regions with different reactivity is sufficiently representative of the global dissolution rate. On the basis of the height differences relative to a reference area on the same cleavage face (Figure 8 top), the absolute rate was calculated to be 3.2×10^{-9} mol m^{-2} sec^{-1} (equation [5]). This value agrees very well with the average dissolution rate calculated.

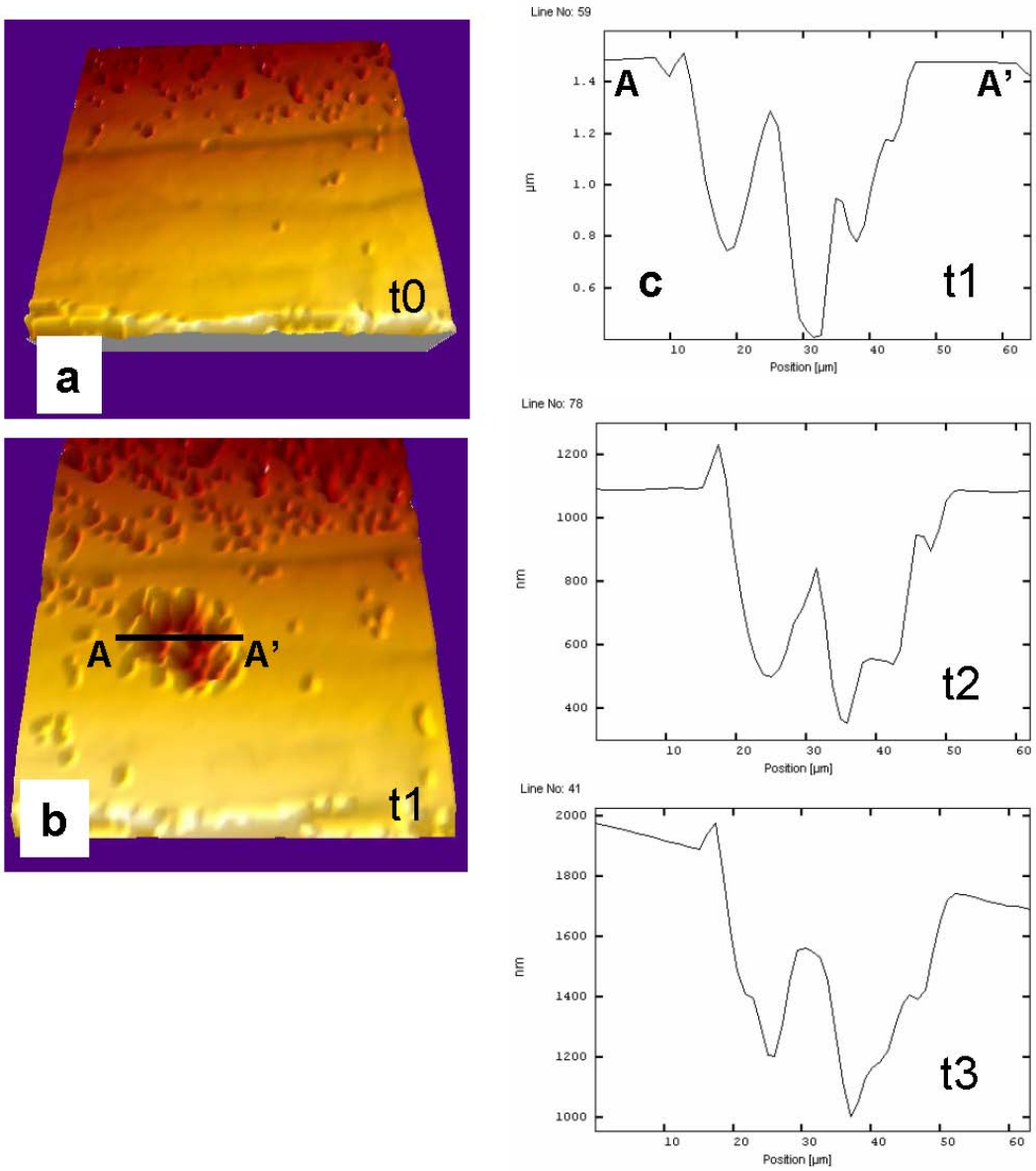

Figure 6. Three-dimensional images of (a) initial surface with different pit density and (b) same reacted surface region after 13 d (t1) showing trains of pit coalescence and annihilation of pits. Images are 120×120 microns. X-line profiles in (c) show the evolution of the formed etch pit over the experimental run.

Pyrite dissolution rate normalized to geometric area – Figure 8 (bottom) shows the variation in Fe output concentration as a function of time in the experiment (1007 h). The iron output concentration remained steady after 500 h up to the end of the experiment. The calculated steady-state dissolution rate was 7.2 ± 1.5×10^{-9} mol m^{-2} s^{-1}, using equation [2], the steady-state output iron concentration (0.53×10^{-6} M), and the estimated geometric surface area. Lüttge (2005) has shown that the rate constants computed from geometric surface area could be distinctly higher than the rate constant derived from reactive surface area, even after extensive dissolution, due to the loss of flat surface area. If we assume here that the rate $r = k_{geo}$ (given the large undersaturation with respect to pyrite), then k_{geo} is higher than k_{react} by a factor of 2.

Comparison with previous experimental dissolution studies – Pyrite bulk rates have been calculated from iron and sulfur released to solution from dissolving pyrite grains and not by direct measurements of changes in the surface topography of crystals. Nordstrom and Alpers (1999) reported that abiotic rates at

similar acidic pH, oxygen saturated atmosphere and 25°C vary between 3×10^{-10} and 3×10^{-9} mol m^{-2} sec^{-1}. These rates were normalized using a BET specific area of 0.025 m^2 g^{-1}. Williamson and Rimstidt (1994) reported dissolution rates at pH 2 and oxygen saturated atmosphere that ranged from 1.2 to 4×10^{-10} mol m^{-2} sec^{-1}. These rates were also normalized using BET specific surface area (0.047 m^2 g^{-1}) obtained from a grain fraction that ranged from 150 to 200 microns. Domènech et al. (2002) and Cama and Acero (2005) obtained dissolution rates for a pyritic sludge (75 % wt. of pyrite) at pH 3 and oxygen saturated atmosphere that were 1×10^{-10} and 6.3×10^{-11} mol m^{-2} sec^{-1}, respectively. These rates were normalized using a BET specific surface area of 1.1 m^2 g^{-1} and a grain size fraction that ranged from 10 to 50 microns. Cama and Acero (2005) obtained rates that were slower by a factor of 1.6 than the rates measured by Domènech et al. (2002). This difference was attributed to the fact that the attainment of steady state before 1000 h, yielded a faster dissolution rate, indicating that the derived rate discrepancy stems from the consideration of an early steady-state condition. Hence, discrepancies between rates measured in bulk dissolution experiments versus direct VSI measurements could reflect different experimental-run times and not BET-specific surface area normalization. Nonetheless, the BET specific surface area is a grain-size dependent parameter. At this point we can suggest that even though the BET surface area is a good proxy for the pyrite reactive surface and suitable for normalizing the bulk dissolution rates, the interferometrically derived rates are independent of particle size altogether, since these are measured by surface retreat of a large, single crystal. Likewise, the use of geometric surface as reactive surface results in a higher apparent pyrite dissolution rate (e.g. by a factor of ~2).

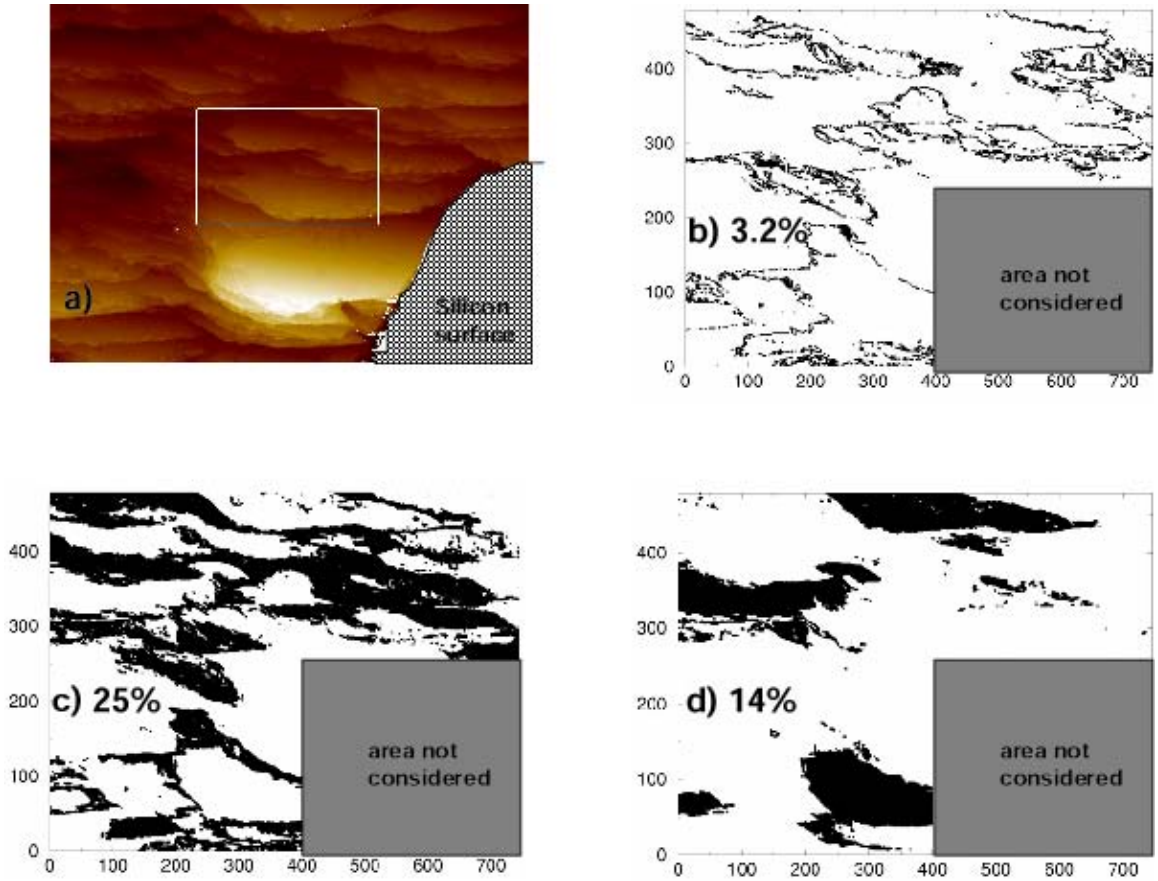

Figure 7. Interferometric data of the pyrite surface (a) and dissolution-rate plots showing the surface regions with distinct reactivity (black areas): (b) 3 % of the total area with $r < 1.7\times10^{-9}$ mol m^{-2} sec^{-1}; (c) 25 % of the total area with $1.7\times10^{-9} < r < 1.7\times10^{-8}$ mol m^{-2} sec^{-1}; (d) 14 % of the total area with $1.7\times10^{-8} < r < 1.7\times10^{-7}$ mol m^{-2} sec^{-1}.

Dissolution of sphalerite (De Giudici et al., 2002), galena (De Giudici and Zuddas, 2001; Cama et al., 2005) and chalcopyrite (Abraitis et al., 2004) was also studied by means of AFM experiments. For galena and sphalerite, dissolution rates were obtained from local surface spots (5×5 microns) and cleavage

surfaces. The in-situ AFM dissolution rates differed from rates obtained by means of flow-through experiments by more than one order of magnitude (Cama et al., 2005). However, in all these studies nucleation and disintegration of S-bearing hillocks controlled the dissolution process. We also observed the existence of such features on weathered surfaces prior to reaction, that disappeared after dissolution (Figure 9). Because these features are not preserved in our experiments, we argue that it is unlikely that they are metastable S-bearing phases. We suggest instead that they are remnant parts of the surface that did not dissolve completely. Considering the spatial and time scales of our VSI measurements, we can neither confirm nor rule out that the previously suggested mechanism governing sulfide dissolution does not apply to pyrite at very acidic conditions.

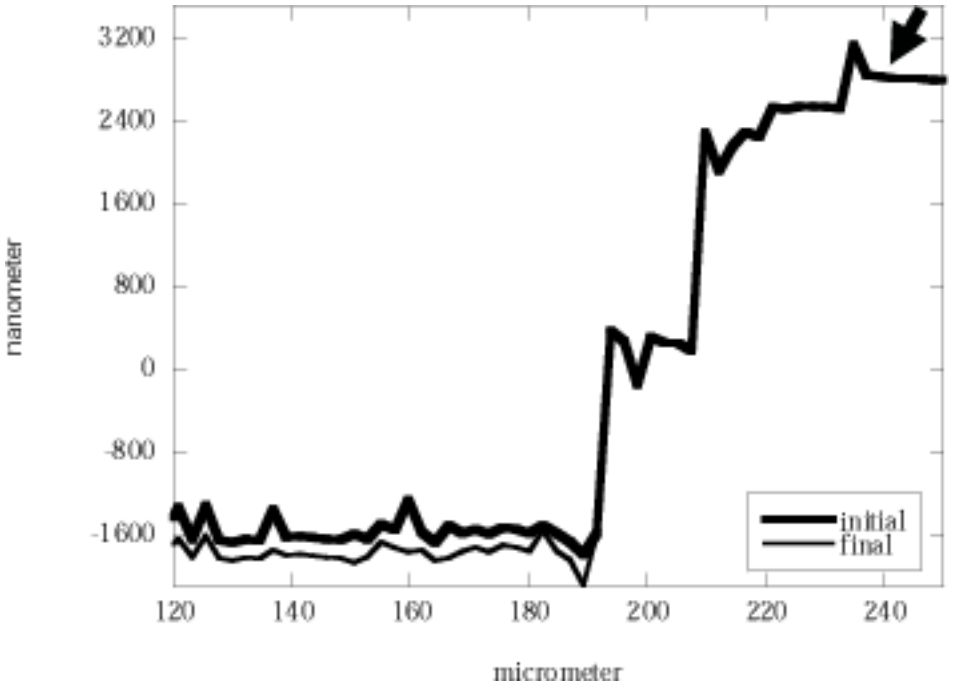

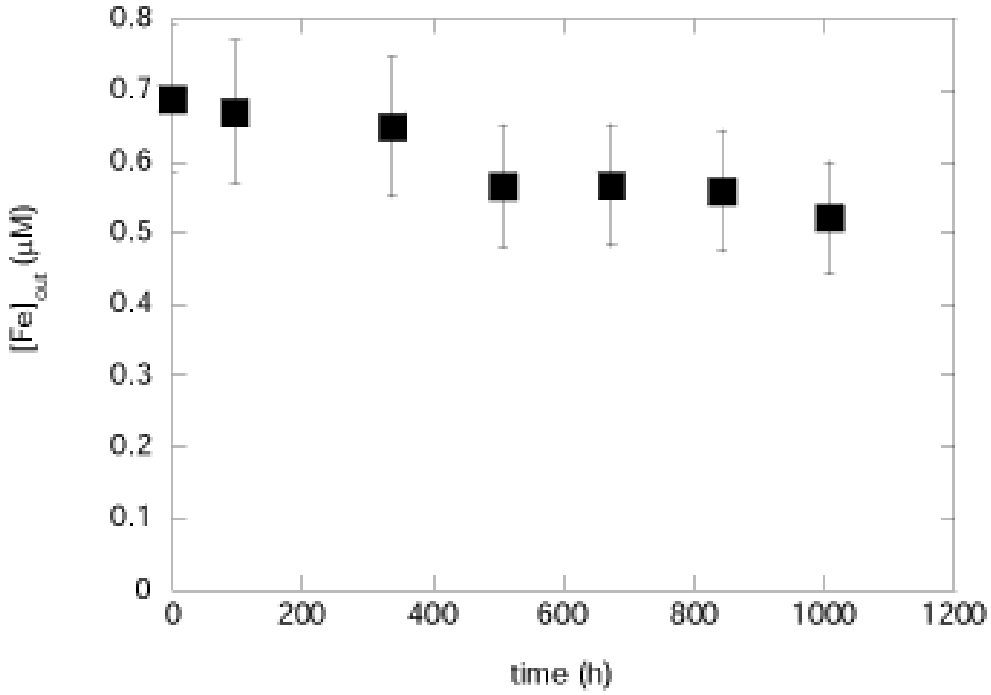

Figure 8. (Top) Profiles that show the surface before (a) and after the reaction (b). The arrow indicates the reference, masked part of the surface where the mask was removed (from 190 to 250 µm). (Bottom) Variation in total iron concentration with time in the flow reactor. Steady state was reached after 500 h of dissolution.

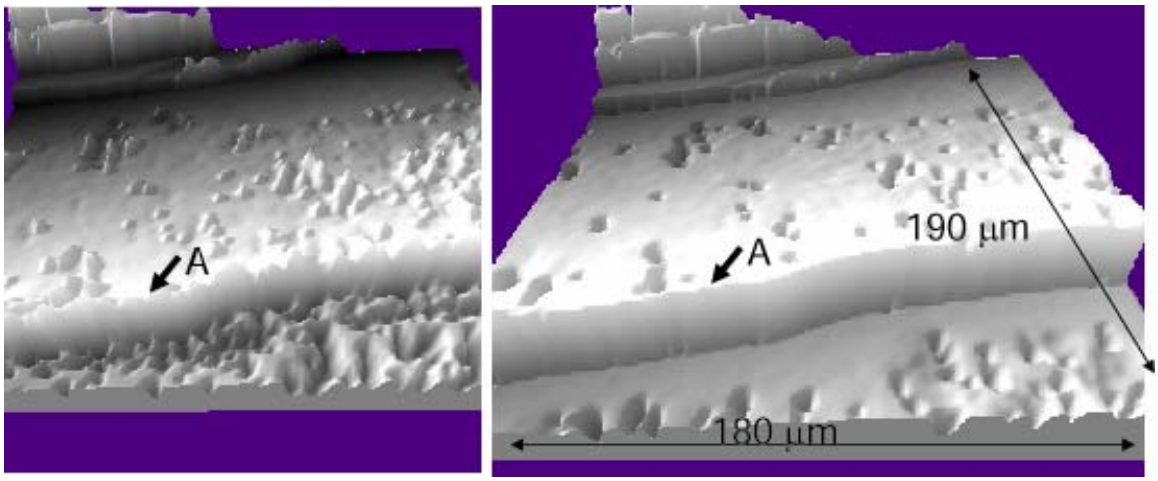

Figure 9. Three-dimensional images of (a) initial portion of the surface with scattered hillocks and (b) reacted surface after 13 d (t1) showing the disappearance of the surface hillocks and the presence of etch pits. Images are 180×190 micrometers. The terrace height in A is 750 nm.

CONCLUSIONS

Vertical scanning white light interferometry was used to study the dissolution of a naturally weathered pyrite surface under laboratory conditions (pH 1, oxygen saturated atmosphere, undersaturation with respect to pyrite, and room temperature) for 27 d (648 h). The metallic character of pyrite provided high light reflectivity, yielding excellent surface images that allow a detailed, high-resolution comparison between the original weathered and experimentally reacted surface. Such long-term experiments are a prerequisite to obtain pyrite dissolution rates that are comparable to weathering of pyrite grains under acid mine drainage conditions. An advantage of using VSI over AFM is its ability to explore surface areas of millimeter size with nanometer precision in height.

The previously weathered pyrite surface consisted of flat regions devoid of etch pits and regions densely pitted. Although variation in surface roughness was essentially negligible this surface morphology could lead to variability in the extent of dissolution.

In the present VSI investigation of pyrite dissolution the stepwave model of the dissolution process, involving the formation of etch pits, the generation of dissolution stepwaves and a resulting overall surface retreat is able to account for the dissolution processes observed. An important finding is that surface reactivity is non uniform over the surface, yielding variation in specific dissolution rates. Rates ranged from 10^{-7} mol m^{-2} sec^{-1} to undetectable rates. The average dissolution rate was 2.8×10^{-9} mol m^{-2} sec^{-1} at pH 1 and agrees with the absolute rate (3.1×10^{-9} mol m^{-2} s^{-1}) as well as with select bulk measurements found in the literature. The pyrite dissolution rate normalized using geometric surface area was $7.2\pm1.5\times10^{-9}$ mol m^{-2} sec^{-1}, i.e., a factor of 2 higher. Nevertheless, these results underscore the necessity of direct measurements as provided by VSI to study pyrite dissolution kinetics.

Current work is underway to study the dissolution of other sulfides using VSI. Detailed inspections of the reacted surfaces should contribute to elucidate further on mechanisms that seem to control sulfide reactivity, such as growth of sulfur-bearing hillocks during the dissolution process as was described in previous studies of sulfide dissolution (De Giudici and Zuddas, 2001; De Giudici et al., 2002; Cama et al., 2005). In addition much more work needs to be done to understand the influence of factors such as ΔG and catalysis of pH, oxygen, Fe(III) and bacteria governing sulfide dissolution in natural environments.

REFERENCES

Abraitis, P., Pattrick, R., Kelsall, G. and Vaughan, D. (2004) Acid leaching and dissolution of major sulphide ore minerals: processes and galvanic effects in complex systems. Mineralogical Magazine, 68(2), 343–351.

Arvidson R.S., Ertan I.E., Amonette J.E., and Luttge A. (2003). Variation in calcite dissolution rates: A fundamental problem? Geochimica et Cosmochimica Acta, 67, 1623-1634.

Arvidson R.S., Collier M., Davis K.J., Vinson M.D. and Luttge A. (2006) Magnesium inhibition of calcite dissolution kinetics. Geochimica et Cosmochimica Acta 70, 583–594.

Beig M.S. and Luttge A. (2006) Albite dissolution kinetics as a function of distance from equilibrium: Implications for natural feldspar weathering. Geochimica et Cosmochimica Acta, 70, 1402-1420.

Bonnissel-Gissinger P., Alnot M., Ehrhardt J-J., and Behra P. (1998) Surface oxidation of pyrite as a function of pH. Environmental Science and Technology 32, 2839-2845.

Cama J. and Acero P. (2005). Dissolution of minor sulphides present in a pyritic sludge at pH 3 and 25ºC. Geologica Acta, 3 (1), 15-26.

Cama J., Acero P., Ayora C., and Lobo A. (2005). Galena surface reactivity at acidic pH and 25ºC based on flow-through and in situ AFM experiments. Chemical Geology, 214, 309-330.

De Giudici G. and Zuddas P. (2001). In situ investigation of galena dissolution in oxygen saturated solution: evolution of surface features and kinetic rate. Geochimica et Cosmochimica Acta, 65, 1381-1389.

De Giudici G., Voltoni M., and Moret M (2002) Microscopic surface processes observed during the oxidative dissolution of sphalerite. European Journal of Mineralogy 14, 757-762.

Domènech, C., De Pablo, J., Ayora, C., 2002. Oxidative dissolution of pyritic sludge from the Aznalcóllar mine (SW Spain). Chem. Geol. 190, 339-353.

Evangelou, V.P., Seta, A.K., Holt, A., 1998. Potential role of bicarbonate during pyrite oxidation. Environ. Sci. Technol. 32, 2084–2091.

Green E. and Luttge A. (2006) Incongruent dissolution of wollastonite measured with vertical scanning interferometry. American Mineralogist 91, 430-434.

Jambor J.L., Blowes D.W., and Ptacek C.J. (2000) Mineralogy of mine wastes and strategies of remediation. In: Environmental Mineralogy. Vaughan D.J. and Wogelius R.A. (eds) EMU Notes in Mineralogy 2, Ëotvös University Press, 255-290.

Jurjovec, J., Ptacek, C.J., Blowes, D.W., 2002. Acid neutralization mechanisms and metal release in mine tailings: A laboratory column experiment. Geochim. Cosmochim. Acta 66, 1511–1523.

Lasaga A.C. and Luttge A. (2001) variation of crystal dissolution rate based on a dissolution stepwave model. Science 291, 2400-2404.

Lowson, R.T., 1982. Aqueous pyrite oxidation by molecular oxygen. Chem. Rev. 82, 461 – 497.

Lüttge A. (2005). Etch pit coalescence, surface area, and overall mineral dissolution rates. American Mineralogist, 90, 1776-1783.

Lüttge A., Bolton E.W., and Lasaga A.C. (1999). An interferometric study of the dissolution kinetics of anorthite: the role of reactive surface area. American Journal of Science, 299, 652-678.

Luttge A., Winkler U., and Lasaga A.C. (2003). An interferometric study of the dolomite dissolution: A new conceptual model for mineral dissolution. Geochimica et Cosmochimica Acta, 67, 1099-1116.

McKibben, M.A. and Barnes, H.L., 1986. Oxidation of pyrite in low temperature acidic solutions: Rate laws and surface textures. Geochim. Cosmochim. Acta 50, 1509-1520.

Moses, C.O. and Herman, J.S., 1991. Pyrite oxidation at circumneutral pH. Geochim. Cosmochim. Acta 55, 471-482.

Nicholson, R.V., Gillham, R.W., Reardon, E.J., 1988. Pyrite oxidation in carbonate-buffered solution: 1. Experimental kinetics. Geochim. Cosmochim. Acta 52, 1077-1085.

Nordstrom D. K. and Alpers C.N. (1999) Geochemistry of acid mine waters. In Reviews in Economic Geology V. 6A, 133-160: The environmental geochemistry of mineral deposits. Part A: Processes, Techniques, and health Issues. Edited by G. S. Plumlee and M.J. Logsdon.

Parker, G., Robertson, A., 1999. Acid Drainage. A critical review of acid generation from sulfide oxidation: Processes, treatment and control. Australian Minerals & Energy Environment Foundation, Occasional Paper No. 11, 227 pp.

Parkhurst, D.L., 1995. User guide to PHREEQC - a computer program for speciation, reaction-path, advective-transport, and inverse geochemical calculations. US Geological Survey Water Resources Investigation Report 95-4227, Lakewood, Colorado, 143 pp.

Rimstidt J. D. and Vaughan D. J. (2003) Pyrite oxidation: A state-of-the-art assessment of the reaction mechanism. Geochimica and Cosmochimica Acta 67, 873-880.

Roso K.M and Vaughan D.J. (2006) Reactivity of sulphide mineral surfaces. In Reviews in Mineralogy V. 61, 557-607: Sulfide Mineralogy and geochemistry. Edited by D.J. Vaughan.

Singer, P.C., Stumm, W., 1970. Acidic mine drainage: the rate-determining step. Science 167, 1121-1123.

Williamson, M.A., Rimstidt, J.D., 1994. The kinetics and electrochemical rate-determining step of aqueous pyrite oxidation. Geochim. Cosmochim. Acta 58, 5443-5454.camg(co3)dmesgCamg(co3)2

Thomas, T. R., 1999. Rough Surfaces: London, Imperial College Press, 278 p.